The Application of a Masked Orbiting Transmission Source for Attenuation Correction in PET

Nicole T. Ranger*, Christopher J. Thompson, and Alan C. Evans

McConnell Brain Imaging Centre, Montreal Neurological Institute and Medical Physics Unit, McGill University

A new technique for attenuation correction in positron emission tomography is introduced and evaluated. Transmission scans are performed with a point source of ^{68}Ge encapsulated in a lead collimator that masks the source into a fan beam in the scanning plane. The source orbits the patient section at the edge of the slice defining collimator. Only events acquired by detector pairs that are collinear with the source are used to calculate the attenuation coefficients. Events from detector pairs that are nearly collinear are rejected, while those from detector pairs that are far from collinear may be used to acquire a simultaneous emission scan. The coincident event rate per unit source activity is over twice that of rod and ring sources. This technique is compared with calculated outline and ring source attenuation correction techniques in a pie phantom. The linear attenuation coefficient for water was measured as 0.096 cm^{-1}, and 0.094 cm^{-1} when the water contained 12 kBq/cc ^{68}Ga, compared with 0.085 cm^{-1} for a ring source. Cerebral glucose utilization rates in a normal volunteer reconstructed with transmission scans performed pre- and postinjection of fluorodeoxyglucose show no significant differences. However, values of cortical glucose utilization average 12% above those measured with the fitted outline method in the highest cuts because of the obliqueness of the skull to the planes examined.

The coincident annihilation photons imaged in positron emission tomography (PET) undergo significant attenuation before emerging from the body section being imaged. When traversing the longest attenuation paths through a head section only about one pair in seven emerges unscattered. In some body sections attenuation factors of 50:1 have been reported (*1*). Thus, attenuation compensation is the most important correction factor to be applied in quantitative PET imaging.

Three common techniques are employed to obtain the necessary correction factors for attenuation compensation, geometric outline, outline fitted around the emission scan, and transmission scans. The first two techniques usually apply a constant linear attenuation coefficient to a measured chord length for each sample of each projection, whereas the transmission scan provides an estimate of the total attenuation coefficient for each chord from the ratio of the event rates recorded from a source before and after the patient enters the field of view. The calculated methods have the advantage of being faster, and entail a lower radiation dose since only an emission scan is performed. They do not account for regional differences in attenuation coefficients in bones and airways compared with soft tissue.

Transmission scans are considered essential for heart studies where there are very large differences in attenuation especially when the patient is not able to withdraw his arms above his head, and out of the scan field of view. Previously the transmission scan had to be performed prior to the emission scan. The patient must be immobilized, or repositioned exactly for correct application of this technique. This prolongs the scanning time especially for fluorodeoxyglucose (FDG)

studies where the uptake phase of the scan may not be required.

The geometric outline technique consists of interactively positioning an ellipse around a PET image presented to a trained operator. The orientation, size, and position of the ellipse are adjusted to "fit" around the displayed image. This technique is subjective and requires user intervention for each of a series of slices. Most head sections are far from elliptical as reference to any set of transaxial x-ray computed tomography scans clearly shows. Errors in the size and shape of the ellipse will result in significant regional errors in tracer estimation (2).

The fitted outline is very commonly used. The fitting was originally done by thresholding an uncorrected image (3), and later on the sinograms during reconstruction (4-7). Tomitami (7) emphasized the importance of estimating the "skull thickness". He points out that an underestimation of this parameter causes all activity concentration values in the slice to be low but the error becomes greater as one approaches the brain-skull interface, with an opposite effect if the skull thickness is overestimated. Since most PET applications require accurate quantification of the cortical mantle, incorrect attenuation in this region has serious ramifications. He also discusses compensation for the higher attenuation coefficient of the skull. To compensate for the increased attenuation one can exaggerate the skull thickness by the ratio of the attenuation coefficients for bone and soft tissue ($\sim$1.6).

Often the skull outline is determined by applying an adjustable threshold to each projection, depending on whether the tracer is present in the scalp, skull, or brain alone. In the present study the threshold was optimized by requiring the calculated head outline circumference to "match" the patient's head circumference at each level studied. Before the scan the patient's head circumference at the lowest level to be scanned, and the distance to the vertex are measured and recorded. The head circumference at each slice is estimated by the reconstruction program assuming the circumference decreases as if the head was an ellipsoid.

The fitted outline technique cannot account for variations in skull thickness at different levels or the effects of lower attenuation through the eyes, temporalis muscles, nasal sinuses, or the higher attenuation in the very dense petrous bones at the base of the skull. A transmission scan is required to accommodate these differences in attenuation.

The linear attenuation coefficients for water and bone at 511 keV are 0.096 and 0.152 cm^{-1} (determined by linear interpolation of values in Johns and Cunningham (8) p:724. A ICRP (9) report on "Reference Man" gives the same attenuation coefficients as 0.094 and 0.174 cm^{-1}. Lower attenuation coefficient values are sometimes used (2,6) to compensate for scattered radiation

present to a varying extent in all PET scanners. An error of 1% in the attenuation coefficient in a 10-cm-long attenuation path yields an error of $\sim$1% in the activity concentration measurement.

Apart from the extra scanning time and radiation dose previously mentioned, transmission scans introduce noise resulting from limited photon statistics and random and scattered events recorded during the transmission scan. The random counts are especially bothersome since one would like to minimize the scan duration, and a high concentration of isotope in the ring source near the detectors gives rise to an abnormally high rate of singles whose coincident mate is absorbed or scattered in the patient section. The random rate is almost constant along any projection whereas the true rate falls as one approaches the longest path through the patient section. Dahlbom et al. (1) have estimated that the random rate in the central part of some projections in a body section may reach five times the true signal rate, making the estimation of the true rate extremely unreliable. Unfortunately, it is through the thickest sections that the transmission scan is most contaminated by random events, and it is there that greatest accuracy is required to estimate the correction in the emission scan.

Carroll (10) introduced the orbiting rod source specifically to reduce random counts. He selectively disabled most banks of detectors which were far from being collinear with an orbiting rod source of germanium-68 (^{68}Ge). Although the single events in detectors near the orbiting source are much higher due to the source being concentrated, all rays reaching the far detector must have passed through the patient, so their rate is proportionately much lower. Since the random event rate is the product of the rates in each detector, the net random event rate is much lower.

An improvement to the technique was proposed for the Donner 600-detector tomograph (11,12) and independently implemented and tested by us (13). In our validation of the rod source technique we used the programmable lookup tables normally used to generate uniformly sampled sinograms (14) on the Positome IIIp (6) to accept only collinear detector pairs. The experiments presented here also use this discrete detector pair selection. The Donner system uses a programmable read only memory (PROM) to identify detector pairs which are precisely collinear with the source as it orbits the patient's head. Events that do not meet the collinearity criterion stored in the PROM are discarded before incrementing the sinogram memory. The post-sinogram selection (12) approach is superior to the discrete detector selection since the sinogram is more finely sampled than the coincident detector pair separation.

In our previous work we used a rod source, as have others using or proposing this technique, but suggested

that results could be improved by using a point source enclosed in a lead source collimator. There are five reasons for this as follows.

1. Figure 1 shows the axial aperture function for the upper direct slice and half of the aperture function for the cross slice at the inner edge of the collimator. Elements of a rod source (shown dotted in Fig. 1) above or below the flat central portion of this aperture function contribute fewer coincident events while their contribution to the singles rate, and thus to the crystal dead time and random rates is independent of position, at least within the opening of the septa. In a multi-slice system, activity in sections of the rod (shown white in Fig. 1) next to the septa is wasted. Thus, a thin source at the peak of the aperture function will give a higher coincident countrate per unit activity than an axially distributed one.

2. Since the source collimator almost fills the gap between the slice defining septa, the crystals near the source are shielded from any radioactive tracer in the patient section under study. In our case the source collimator is 2 cm in diameter giving up to a 16-fold attenuation for all but the flat slit containing the source.

3. The opening in the source collimator is in the form of a fan, both in front of and behind the source, attenuating the beam for detectors outside the field of view. This in turn reduces their unwanted singles count-rate and deadtime, freeing them to accept emission events from the patient section under study with minimum random rates, thereby offering the possibility of performing simultaneous transmission and emission scans.

4. If the axial extent of the detectors in the direct and adjacent cross planes is projected through a point source and onto the near crystal face (dotted lines in Fig. 1), it can be seen that not all the rays directed towards the nearer detector will have coincident mates which could ever reach a detector on the far side. By collimating the

source with lead, one can attenuate the unwanted portion of the beam illuminating the near detector, that will decrease its deadtime and random rate without loss of coincident counts.

5. The sub-collimator provides a degree of self shielding to reduce the radiation exposure to the technicians who must install and store the source before and after each use.

Recently Daube-Witherspoon et al. (15,16) suggested that transmission scans could be performed "postinjection" by first performing the emission scan, followed by a rod source transmission scan. They found it necessary to subtract ~5% of the (half-life corrected) estimate of the emission data before calculating the attenuation. The method we utilize does not require partial subtraction of the emission events since encapsulation of the flat source in lead shields detectors near the orbiting source from gamma rays from the tracer in the patient slice.

The proposed masked orbiting transmission source (MOTS), masked both mechanically by the lead collimator into a flat fan beam, and electronically by only allowing detector pairs collinear with it to be selected for the attenuation scan, allows most detector pairs not involved in acquiring the transmission scan to acquire a simultaneous emission scan.

MATERIALS AND METHODS

The present studies were carried out on the Positome IIIp two ring tomograph at the Montreal Neurological Institute (3,6,14). It has an in-plane resolution of 11mm and slice thickness of 16 mm full width of half maximum (FWHM) with a slice separation of 18 mm.

Simulation of Transmission Sources

Monte Carlo simulation techniques (17) were used to determine the coincident and total count rates for four different transmission source geometries. The simulations are similar

FIGURE 1

Comparison of rod and MOTS transmission scan sources in the Positome collimators. The axial aperture function for the rod source at the edge of the collimator (at left) is shown for the direct slice (above) and for the top half of the cross slice (below). Some of the activity is wasted in the rod source. The MOTS source on the right is within the maximum of the axial aperture function. The dotted lines extending to the detector show the portion of it exposed to potentially coincident gamma rays. The vertical scale is twice the horizontal scale for clarity.
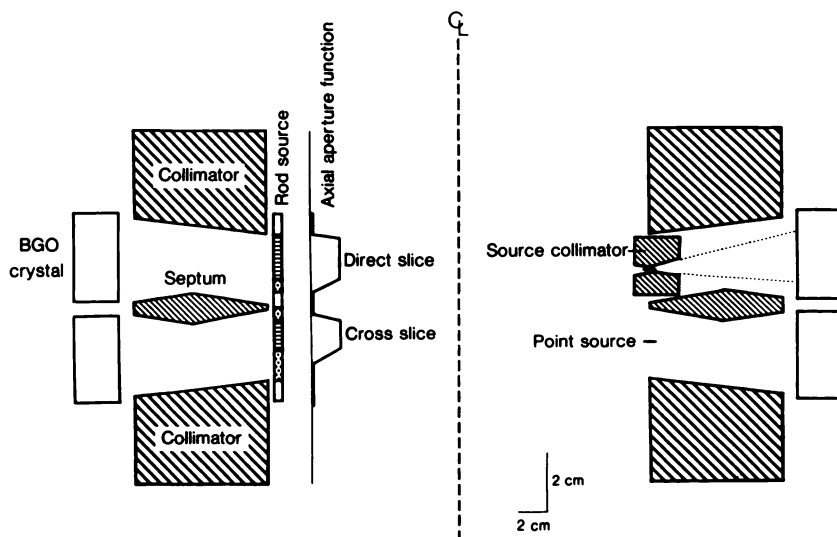
to a blank scan, since all countrates are highest in this case. All sources fit just inside the 25 cm diameter collimator opening. The following source geometries were simulated.

1. A water-filled ring source with inner and outer diameters of 11.8 and 12.3 cm, 6.5 cm high.

2. A water filled 0.3-cm-diameter rod source 6.5 cm high with an orbit radius of 12 cm.

3. Two point sources with an orbit radius of 12 cm, each centered in a detector plane.

4. Sources as in three but sandwiched between 2 × 2 cm lead blocks with a 2-mm gap.

The last source geometry is the closest approximation to the actual source geometry permitted by the simulation program, which restricts off axis shielding materials to nested rectangular blocks. Since it does not include the wedge shaped lead pieces (Fig. 2) that shield the detectors outside the field of view, this will overestimate the singles rate, but not effect the coincident rate.

The following quantities were determined.

1. The counting efficiency of the source geometry expressed as coincident count rate per unit total transmission source activity within a 20-cm field-of-view. (This size was chosen since most of these events would be detected on chords through an actual patient's head).

2. The total singles + coincident count-rate per unit source activity.
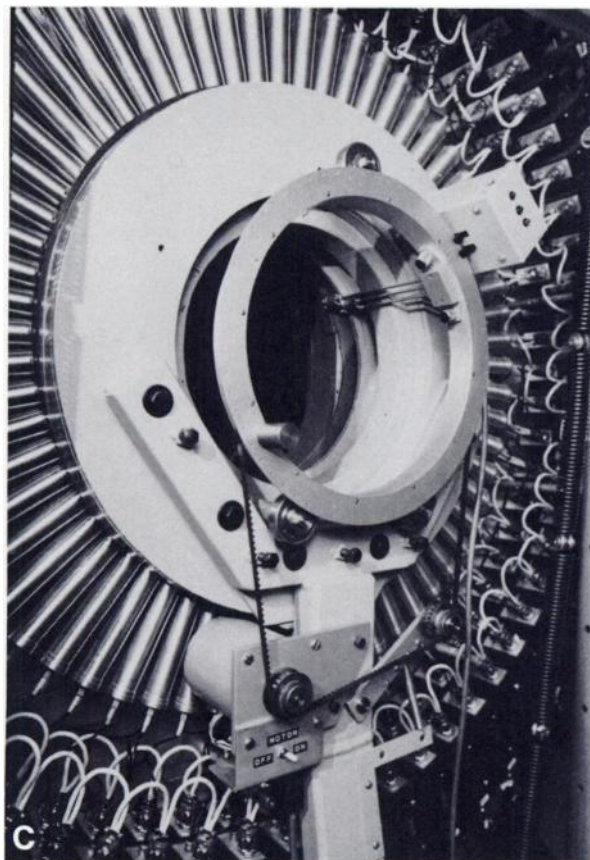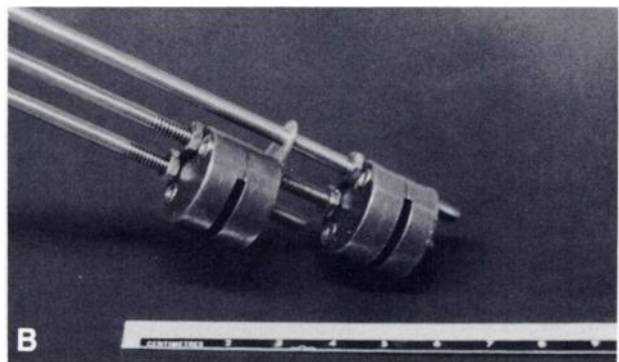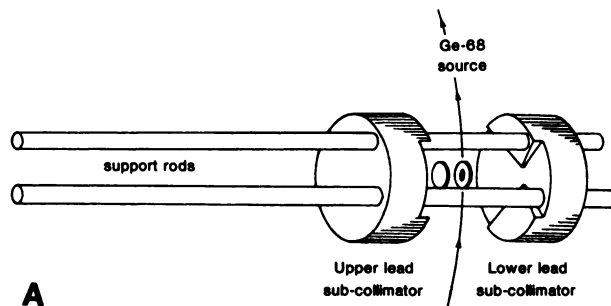
FIGURE 2

A: Details of transmission source, lead collimator and support rods. B: The two sources fully assembled. C: Rear view of Positome showing sources and orbiting drive assembly.

3. The ratio of total to coincident count rates from which the random fraction can be calculated for a given source strength.

4. The total event rate for the nearest detector (from which the relative detector live time can be estimated).

Implementation of the Transmission Source

Two 37-MBq (at time of manufacture) sources of electroplated ^{68}Ge were formed as 3-mm-diameter dots in the center of 0.5 mm-thick, 5-mm-diameter nickel disks. An identical disk was attached with epoxy cement to cover each source. Uncovered sources like this are commercially available (The sources were fabricated by Dupont Company, No. Billerica, MA) and are often used as positron sources for metallurgical studies.

Encapsulation of the sources in nickel prevents risk of contamination while handling the sources, and ensures that all the positrons annihilate within a very small distance eliminating the positron range blurring of other aqueous or gel preparations of ^{68}Ge.

The lead source collimators that surround the source and shape the distribution of coincident radiation into a flat fan beam are shown in Figure 2A. The two support rods for each source provide a unique source orientation so that the "blank field" scan need only be done every few weeks, as dictated by the tomograph's stability, rather than by changes in source geometry.

In our tomograph the two detector arrays are staggered by half a crystal width, therefore the two sources are offset by a proportional amount. The source collimators are shown fully assembled in Figure 2B.

The complete source assembly is attached to the inside of a thin rotating drum with two knurled screws. The sources orbit on opposite sides of the slice defining septum at a radius of 12.7 cm. The drum is rotated by a stepping motor driving a timing belt, as shown in Figure 2C. A series of 64 holes sensed by an optical encoder indicate the location of the source as it passes each detector position. A second optical encoder senses reference positions corresponding to the source at "detector 0" and the removal point, just above the patient's head rest.

The source movement is under computer control. It can move a preset number of steps, to the next detector, to the reference detector (prior to the start of a scan), or to its removal point (on completion of the transmission scan). The source is installed, removed, and stored manually.

In all studies reported here the source was stepped from detector to detector while the data translation tables were loaded with a new set of collinear detectors. Data was collected for a preset time, usually 8 sec with a wobble period of 2 sec. While this process wastes 20% of the time and counts, it has provided valuable insight into the optimal detector pair selection without the need to replace, erase and reprogram a PROM, since the data translation tables are implemented as dual-ported memory in CMOS static random access memories (14). For the blank field scan each of the 64 detectors was sampled four times, for a total scanning time of 8 × 64 × 4 sec. In all cases a blank field scan was done within 2 wk of the study.

A ring source in the form of a spiral of ten wraps of plastic tubing on a thermoplastic former that fits snugly into the collimator opening was used to perform ring source transmission scans. The tubing was filled with ~10 MBq of gallium-68 (^{68}Ga) ethylenetriaminetetraacetic acid (EDTA). A blank field scan was always performed first, followed as soon as possible by the attenuation scan. The scan time in each case was 10 min.

Data Treatment for Attenuation Scans

Each raw data set is a sinogram of 64 uniformly sampled (at five samples/cm by the address translator) parallel projections. It is corrected for isotope decay back to the time of first use, and scaled for the decay-corrected counting time of each scan. A point at sample number i, of projection j, in a new sinogram A_{ij} is related to a point in the corrected blank field sinogram B_{ij} and the transmission T_{ij} by:

$$A_{ij} = 2000 \ln [B_{ij}/T_{ij}].$$

The scaling factor 2,000 (the product of 0.2 cm/pixel and 10,000) causes the reconstructed image to be scaled in units of 10,000/cm. Quantitative attenuation scans can thus be obtained in units such that the true value for the linear attenuation coefficient for water (0.096 cm^{-1}) reads out as 960 attenuation units.

The attenuation sinograms are reconstructed by the same program used to reconstruct activity concentration data with the calibration, scatter, and attenuation corrections disabled. No random count-rate or deadtime corrections are performed on the attenuation data. Almost all the random events and detector deadtime are the results of single events from parts of the source close to the detectors. For the ring source studies, these rates change by only 15% between ^{68}Ga studies done 10 min apart, and the reduced random rate during the transmission scan would tend to increase the attenuation coefficients in the ring studies. As we shall see, the attenuation coefficients are always lower for the transmission scans using a ring source. The random count-rates in all transmission scans were always <5%.

Data Treatment for Emission Scans

The attenuation sinograms from either ring or MOTS scans can be used to perform the attenuation correction on the emission sinograms E_{ij} by scaling as:

$$C_{ij} = E_{ij}e^{[A_{ij}/2000]},$$

where C_{ij} is the attenuation corrected sinogram. This scaling is done after calibration, randoms, and deadtime compensation and scatter deconvolution, but prior to image reconstruction using the filtered backprojection method. The scatter filter is adjusted to the equivalent slice diameter (defined as the length of the attenuation outline perimeter divided by π) by fitting of its coefficients as previously described (5,6). When a transmission-based attenuation correction is performed the equivalent slice diameter is determined by thresholding the attenuation sinogram. When reconstructing scans using the ring attenuation sinograms the scatter deconvolution was disabled, since both emission and transmission scans have been shown to contain approximately equal scatter distribution (18,19). In this situation the presence of uncorrected scatter in the transmission data acts as a crude scatter correction for emission data similarly left uncorrected for scatter.

Experimental Procedures

In order to demonstrate the effectiveness of this new transmission source geometry several experiments were performed. These were designed to demonstrate the reduction in recorded scattered radiation, and the effects of regional differences in attenuation on observed activity concentrations in emission scans. These tests were done both with and without activity in the scanned volume in order to assess the effect of activity in the scan field on the measured attenuation values.

Effect of regional attenuation coefficient differences on emission scans. A six-sector pie phantom 15 cm in diameter and 10 cm long was used to assess the effect of regional differences in attenuation on the quantification of emission scans. Air was trapped in sector 1; sectors 2, 4, and 6 were filled with distilled water; while sectors 3 and 5 were filled with MD-76 (Mallinckrodt, Pointe Claire, Quebec) an x-ray contrast agent containing 38% iodine in solution. This solution has an attenuation coefficient almost as high as bone at 511 keV. This density pattern is an exaggerated version of a head section through the eyes with the regional density differences because of the nasal sinus and petrous bones.

Transmission scans were performed on this phantom using the ring and MOTS techniques. The water in sectors 2, 4, and 6 was replaced with identical [^{68}Ga]EDTA solutions of specific activity 12 kBq/cc (measured in a well counter at the start of scan). Immediately after a 10-min emission scan a second MOTS transmission scan was performed with the ^{68}Ga still present.

Attenuation sinograms from both the ring and MOTS transmission scans were derived as in the previous study. These were reconstructed into attenuation images. The emission image was reconstructed four ways: (a) with a circular attenuation outline, with the MOTS attenuation sinograms obtained (b) before and (c) after the addition of ^{68}Ga, and with (d) the ring attenuation sinogram and the scatter compensation disabled. A contour profile (with a diameter of 9.5 cm) and 0.6 cm thick was used to plot both the observed activity concentration and linear attenuation coefficients as a function of angle. The contour profiles from all three slices were averaged. These images were reconstructed allowing for negative activity concentration values.

Glucose utilization studies in a normal subject. This study was performed to assess the effect on observed regional glucose utilization rates when using emission outline, ring, and MOTS transmission scans to correct for attenuation.

A normal healthy 23-year-old male subject was fitted with a foam head mold with the scanning plane parallel to the inferior orbital-meatal (OM) line. While the mold was curing a blank field ring source scan was performed. The subject was then installed in the scanner with the lower slice at 3 mm above OM line. A series of four 10-min three-slice ring transmission scans were then done yielding scans at 3, 12, 21, 30, 39, 48, 57, 66, 75, 84, 93, 102 above the OM line. A series of four MOTS scans was then performed in the same couch positions.

A catheter was inserted into the subjects' radial artery and 190 MBq of FDG was injected to the right radial vein while the uptake of the FDG was recorded for 40 min after injection. Timed blood samples were taken rapidly at first and slowly later. The FDG concentration in the plasma was counted and half-life corrected back to the time of injection. Following the uptake phase a set of four static 10-min studies was performed at the same couch positions as the transmission scans. At the end of this set of scans four more MOTS transmission scans were performed in the same couch positions as before. The couch repositioning tolerance is 1 mm so the maximum registration error in the studies is 2 mm in slices with a nominal thickness of 16 mm FWHM.

The subject was then positioned in the same head mold in a Philips 1.5 Tesla Gyroscan Magnetic Resonance Imager (MRI). MRI slices at the same levels and angulation were converted to "PET compatible" images and a template of standard regions of interest (ROIs) was adjusted to match this subjects' MRI scans as described by Evans et al. (*20*).

All three sets of transmission data were converted to attenuation sinograms as previously described. The FDG static emission scans were reconstructed using five different methods of attenuation correction: (a) using an outline fitted to the emission data with the MOTS attenuation scans (b) before and (c) after FDG injection, (d) using the ring attenuation scans with the scatter compensation disabled, and (e) using an outline fitted to the MOTS attenuation scan.

The reconstructed images were combined with the plasma concentration data to obtain regional glucose utilization maps. The ROIs initially established on the MRI planes, were placed identically over the five sets of PET images in turn and regional glucose utilization values were recorded for statistical analysis. The top 50% of the pixels in the MRI defined regions and gray matter rate constants (*21*) were used for gray matter and mixed regions. The bottom 50% of pixels in the MRI defined region, and average white matter rate constants were used for white matter regions.

RESULTS

Simulation of Transmission Source Geometries

The results of the Monte Carlo simulations of various transmission sources are given in Table 1, and the axial geometry and aperture functions for rod and MOTS sources are shown in Figure 1. The ring and rod sources provide almost the same coincident count efficiency. Since the point and MOTS have their activity concentrated at the peak of the axial response function, they yield about 2.3 times more coincident counts per unit source activity. The total event rate for all sources is almost the same, except for a 15% increase for the point sources. This increase is because none of the activity

TABLE 1
Relative Coincident and Singles Countrates for Various Transmission Sources

	Ring	Rod	MOTS	Unshielded point sources
Coinc rate/MBq	1.9 kcps	2.0 kcps	4.7 kcps	4.8 kcps
Total rate/MBq	43 kcps	45 kcps	45 kcps	52 kcps
Total/coinc. ratio	23	22.5	9.5	10.2
Nearest detector count-rate/MBq	700 cps	2.3 kcps	2.7 kcps	3.8 kcps

in the source is shielded from the detectors by lead (Fig. 1).

The improved efficiency of the MOTS and point sources yields a more than twofold improvement in total-to-coincident count ratio. Thus, for a given coincident rate the random rate is reduced over four times. The nearest detector event rate is three to five times higher for the orbiting sources compared to a ring source. For a given coincident count-rate the higher efficiency of the MOTS technique improves the live time of the nearest detector compared to the rod source.

Measurement of Activity Concentration with Regional Attenuation Changes

The transmission scan gray scale images from the pie phantom experiments along with a key to identify regions of the phantom are shown in Figure 3A. All gray scale images are scaled to a common maximum value. The appearance of the two MOTS studies (labeled A and B) are similar whereas the ring source study appears darker implying a lower observed attenuation coefficient. This is quantified in Figure 3B in which the attenuation profiles along a circular contour with a diameter of 9.5 cm are plotted. The average attenuation value for all three water regions is 0.095 cm^{-1} for scans performed without activity in the phantom (labeled "MOTS-before" in Fig. 3B) and 0.094 cm^{-1} with 11.8 kBq/cc present (MOTS-after). The average attenuation coefficient observed for the water regions with the ring source scans is 0.085 cm^{-1}. There is an even greater difference between the MD-76 regions for MOTS and ring source measurements 0.135 and 0.115 cm^{-1}, respectively. The contour profiles for the MOTS-before and MOTS-after scans agree well, while the ring source profile is quite distinct.

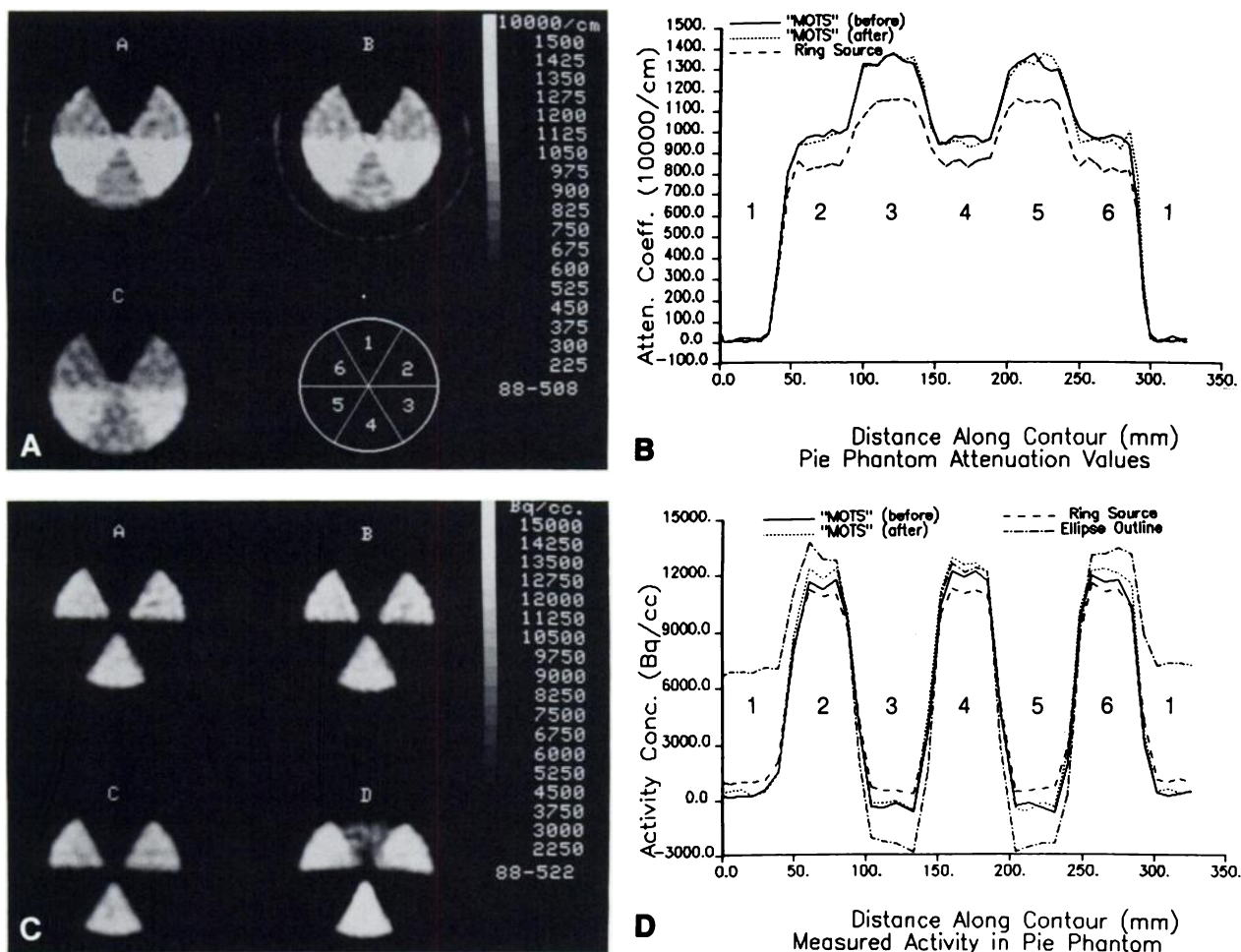Gray scale images of the activity concentration in the

FIGURE 3

A: Transmission scans of pie phantom using A: MOTS without isotope in phantom, B: MOTS with Ga-68 in regions 2, 4 and 6, and C: Ring source techniques. Region 1 contains air, and regions 3 and 5 contain MD-76 iodine contrast agent. B: Contour plots of attenuation coefficients through six regions of the pie phantom. C: Emission scans of pie phantom containing ^{68}Ga solution in regions 2, 4, and 6 only. The attenuation correction is performed by A: MOTS without isotope in phantom, B: MOTS with ^{68}Ga present, C: ring source, and D: calculated circular outline techniques. D: Contour plots of observed activity concentration in emission scans on pie phantom.

pie phantom using the four attenuation correction techniques are displayed in Figure 3C. When a uniform attenuation is used, activity from hot regions is smeared into the "air" region. The activity contour profiles along a circular contour in Figure 3D demonstrate other features as well. Note that negative activity concentrations appear in the regions of highest attenuation. The contour profile for the ring source corrected scans shows activity concentrations of ~1,000 Bq/cc in the air region. This is attributable to scatter in the emission scan, since the scatter compensation is disabled during reconstruction of these scans. Clearly the scatter in the ring transmission scan cannot adequately correct for scatter due to regional variations in isotope distribution in an emission scan, even though it may be approximately correct for a uniform isotope distribution.

In general the activity concentration profiles for the MOTS before and after studies are in excellent agreement except for a 5% overestimation in the active regions. The ring source corrected scan underestimates the activity concentration by about the same amount.

Measurement of Regional Attenuation Coefficients in a Normal Subject

The reconstructed transmission scans for three slices at 3, 48, and 93 mm above the OM line together with the corresponding MRI slices are shown in Figure 4. In spite of the use of a customized head mold there is a clearly observable mis-registration of the "MOTS-before" and ring source transmission scans that were done before the installation of an arterial catheter, and the "MOTS-after" study. From the difference in appearance of the nasal sinuses the subject's head was tilted down slightly during the "MOTS-after" study. All the transmission scans are scaled to a common maximum attenuation coefficient. The images from the ring

source study show lower attenuation coefficients both in the brain, and in the skull. At 511 keV there is a negligible difference in attenuation between the brain and CSF. However, the contrast between bone and soft tissues, especially in the MOTS scans, provides localizing features particularly useful in verifying registration with the emission scans. Average attenuation coefficients for 4-cm-diameter circular brain regions (as far as possible from any bone) in all slices are shown in Figure 5, quantifying the visual differences noted in the images in Figure 4. The error bars show the standard deviation in all the pixels within the ROI. The average brain attenuation coefficients are 0.096, 0.092, and 0.083 cm^{-1} for the preinjection, postinjection and ring source scans, respectively. The average activity concentration in the 12 slices at the time of the MOTS-after scan was between 4 and 7 kBq/cc, and the maximum gray matter value ~13 kBq/cc.

Measurement of Regional Glucose Utilization in a Normal Subject

The glucose utilization scans reconstructed for three slices at 3, 48, and 83 mm above the OM line using the different attenuation correction techniques are shown in Figure 6. All the scans are scaled to a common maximum value of 40 μmol/100g/min.

In the lowest slices the eyes and optic nerves are clearly visible in scans reconstructed with a fitted attenuation outline, but not when a transmission scan is used. The slice at 48 mm above the OM line is generally similar in appearance for all attenuation correction methods. There is a slightly greater contrast in the MOTS corrected studies. All transmission scan corrected studies appear slightly noisier. The white matter of the centrum semi-ovale in the upper slice has a higher apparent glucose utilization in the ring source attenua-
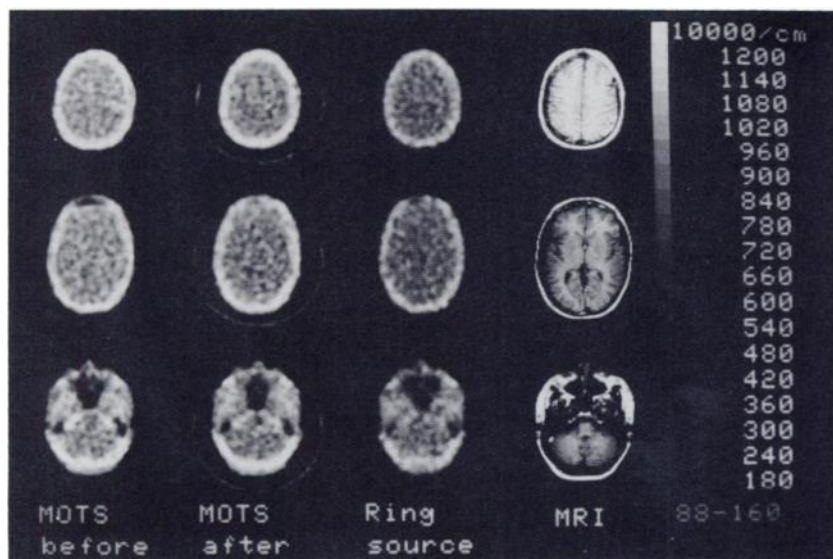

FIGURE 4
Attenuation scans at 3, 48, and 83 mm above the OM line from a volunteer using MOTS pre-injection, MOTS postinjection, and ring source techniques compared with the corresponding MRI slices.
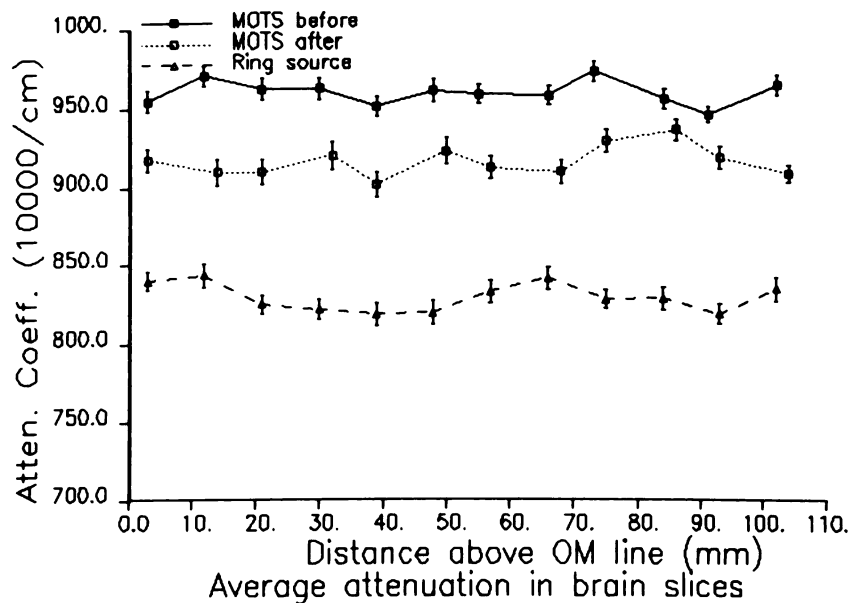
FIGURE 5
Measured attenuation coefficients in a 4-cm-diameter brain region as a function of distance above OM line in scans shown in Figure 4. The error bars are standard deviations of all pixels in the ROI.

tion corrected study because of a lack of compensation for scatter.

The glucose utilization rates and standard deviations (based on the pixels extracted from the MRI-based ROI) are shown for each structure and each attenuation technique in Tables 2 and 3. The noise in the transmission scans is propagated into the emission scans resulting in higher standard deviations in the three reconstructions using transmission scans. Table 2 shows the regional values for a slice 3 mm above the OM line. Regional values for the eyes are much lower in the images corrected with transmission data as a result of the reduced attenuation in the nasal sinus. A regional analysis of the structures in a slice 83 mm above the OM line is presented in Table 3. The average measured gray matter values for glucose utilization are higher by 3% to 10% for reconstructions using transmission data.

This increase is due to the outer gray matter only. Midline structures, (cingulate gyrus and pre-cuneus) are very slightly lower. The white matter in the centrum semi-ovale in the MOTS corrected studies has a lower apparent glucose utilization, while higher values are observed for the ring source corrected studies. The lack of scatter compensation has reduced the contrast. The scatter fraction in this slice was 26%.

Tables 2 and 3 give the average glucose utilization values for gray and white matter for one slice as well as the regional values. From similar data in all 12 slices the average gray and white matter values for all five attenuation correction techniques were extracted and plotted against distance above the OM line in Figure 7. The error bars represent the average of the standard deviations of individual regions. Only one error bar per attenuation technique is drawn for clarity. There is a
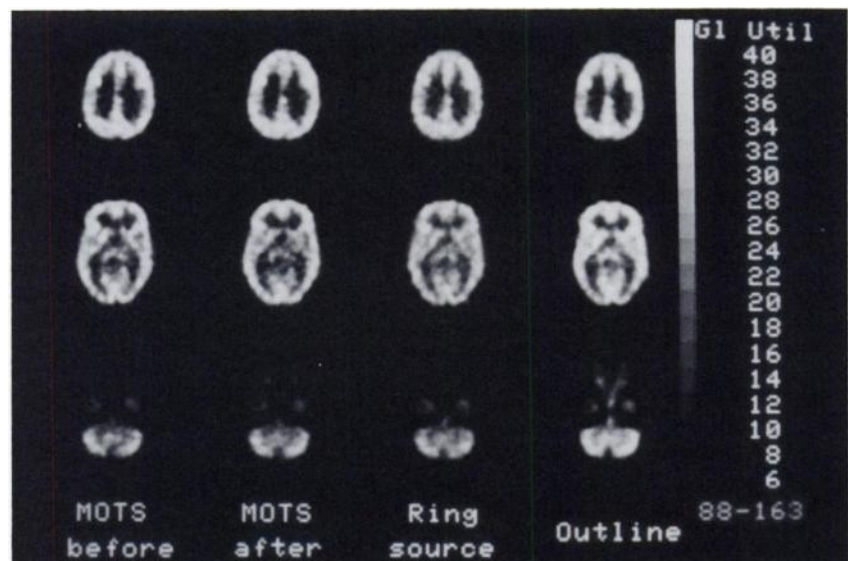

FIGURE 6
Glucose utilization scans at 3, 48, and 83 mm above from a volunteer reconstructed with four attenuation correction techniques.

TABLE 2
Regional Glucose Utilization with Five Different Attenuation Correction Techniques in a Slice 3 mm Above the OM Line

S1:	No.	Emiss Outl	MOTS-pre	MOTS-post	Ring scan	MOTS Outl	Side-structure
1	1	29.5 ± 2.2	27.8 ± 2.8	27.8 ± 3.3	25.6 ± 2.4	27.9 ± 2.1	L-Cerebellum
1	2	19.8 ± 1.4	13.8 ± 1.1	13.7 ± 1.3	15.2 ± 1.1	17.7 ± 1.2	L-Basis pontis
1	3	14.5 ± 1.8	13.5 ± 0.8	12.9 ± 1.4	13.1 ± 1.0	13.1 ± 1.7	L-Basal temporal
1	4	19.0 ± 0.6	7.3 ± 1.2	12.4 ± 1.1	7.0 ± 0.6	15.5 ± 0.5	L-Eye
1	5	29.4 ± 2.2	27.0 ± 2.8	27.4 ± 3.0	24.7 ± 2.2	27.7 ± 2.1	R-Cerebellum
1	6	22.2 ± 0.5	14.9 ± 0.3	16.8 ± 1.0	17.1 ± 0.5	19.6 ± 0.4	R-Basis pontis
1	7	17.9 ± 1.0	15.7 ± 1.0	15.6 ± 0.7	14.8 ± 1.2	16.0 ± 1.0	R-Basal temporal
1	8	16.2 ± 0.3	6.1 ± 0.4	8.3 ± 1.2	4.3 ± 0.2	12.8 ± 0.2	R-Eye
Ave	8	21.0 ± 1.3	15.8 ± 1.3	16.9 ± 1.6	15.2 ± 1.2	18.8 ± 1.1	Slice averages (mixed gray/white)

generally increasing trend in the measured gray matter values with distance in all studies. The lower slices contain many structures characterized as "mixed" and these are combined with the gray matter structures in the regional analysis. The trend is more pronounced in images corrected with MOTS transmission data. This difference is probably because of the apparent increase in skull thickness for transaxial gamma rays near the top of the skull. The dip in observed white matter values near 80 mm above the OM line occurs where the centrum semi-ovale is best resolved as a distinct structure. Note that the white matter values are always higher in the ring source corrected scans showing the reduced contrast when one assumes that the scatter in the emission scan can be compensated by scatter in the transmission scan.

TABLE 3
Regional Glucose Utilization with Five Different Attenuation Correction Techniques in a Slice 83 mm Above the OM Line

| S1:	No.	Emiss Outl	MOTS-pre	MOTS-post	Ring scan	MOTS Outl	Side-structure
10	1	31.9 ± 2.3	34.4 ± 2.4	35.7 ± 2.5	33.1 ± 1.9	31.3 ± 2.5	L-Superior frontal gyrus
10	2	33.1 ± 0.9	35.1 ± 0.7	38.8 ± 0.9	35.5 ± 1.4	33.8 ± 0.9	L-Anterior middle frontal gyrus
10	3	36.8 ± 1.9	39.5 ± 2.3	39.3 ± 1.4	36.6 ± 1.5	37.9 ± 1.8	L-Posterior middle frontal gyrus
10	4	30.0 ± 2.7	31.8 ± 3.2	34.3 ± 2.9	31.4 ± 2.7	31.5 ± 2.7	L-Precentral gyrus
10	5	27.1 ± 1.0	32.1 ± 1.8	32.1 ± 2.3	31.2 ± 2.5	29.3 ± 1.2	L-Postcentral gyrus
10	6	30.0 ± 1.4	35.9 ± 2.0	38.4 ± 2.4	34.8 ± 1.8	32.7 ± 1.5	L-Anterior parietal gyrus
10	7	32.2 ± 2.2	37.9 ± 2.4	38.2 ± 3.1	35.9 ± 1.6	34.8 ± 2.2	L-Middle parietal gyrus
10	8	32.5 ± 1.8	35.7 ± 1.4	37.4 ± 1.8	34.4 ± 1.5	34.5 ± 1.8	L-Posterior parietal gyrus
10	9	36.7 ± 3.4	39.3 ± 3.3	40.1 ± 3.2	38.6 ± 3.6	38.1 ± 3.4	L-Cuneus
10	10	28.0 ± 3.6	27.7 ± 2.8	27.4 ± 4.1	27.3 ± 3.6	27.8 ± 3.6	L-Cingulate gyrus
10	11	37.3 ± 2.3	36.8 ± 2.1	34.6 ± 2.9	34.9 ± 2.4	37.8 ± 2.5	L-Precuneus
10	12	9.0 ± 1.4	6.2 ± 2.3	6.7 ± 2.1	10.6 ± 1.8	8.9 ± 1.4	L-Centrum semiovale
10	13	32.8 ± 2.4	33.6 ± 2.6	34.9 ± 2.5	34.9 ± 2.9	31.5 ± 2.7	R-Superior frontal gyrus
10	14	35.6 ± 1.5	37.4 ± 1.9	39.0 ± 1.6	36.8 ± 1.2	35.2 ± 1.6	R-Anterior middle frontal gyrus
10	15	37.6 ± 1.3	39.8 ± 1.9	41.4 ± 1.7	36.9 ± 1.1	37.6 ± 1.3	R-Posterior middle frontal gyrus
10	16	36.2 ± 3.1	37.4 ± 3.0	38.7 ± 3.6	35.5 ± 2.6	36.5 ± 3.1	R-Precentral gyrus
10	17	30.0 ± 1.6	32.8 ± 2.6	34.1 ± 2.9	30.4 ± 1.3	30.8 ± 1.8	R-Postcentral gyrus
10	18	30.2 ± 1.5	32.0 ± 1.6	34.2 ± 1.4	30.2 ± 1.8	31.2 ± 1.6	R-Anterior parietal gyrus
10	19	31.8 ± 3.1	34.8 ± 3.6	37.0 ± 3.6	32.2 ± 3.4	33.0 ± 3.2	R-Middle parietal gyrus
10	20	30.3 ± 3.5	33.8 ± 3.6	35.7 ± 3.9	33.6 ± 2.8	31.7 ± 3.6	R-Posterior parietal gyrus
10	21	33.5 ± 2.1	36.0 ± 1.8	37.6 ± 1.8	34.7 ± 1.7	34.7 ± 2.1	R-Cuneus
10	22	31.1 ± 3.9	30.1 ± 5.6	28.4 ± 3.7	31.3 ± 3.2	31.0 ± 3.8	R-Cingulate gyrus
10	23	32.1 ± 3.3	31.2 ± 4.1	29.4 ± 4.0	32.0 ± 2.9	32.4 ± 3.4	R-Precuneus
10	24	9.9 ± 1.7	7.4 ± 2.5	8.2 ± 1.8	11.3 ± 1.7	10.1 ± 1.8	R-Centrum semiovale
No.:	22	32.6 ± 2.3	34.8 ± 2.6	35.8 ± 2.6	33.7 ± 2.3	33.4 ± 2.4	Slice averages (gray matter)
No.:	2	9.5 ± 1.6	6.8 ± 2.4	7.5 ± 2.0	11.0 ± 1.8	9.5 ± 1.6	Slice averages (white matter)
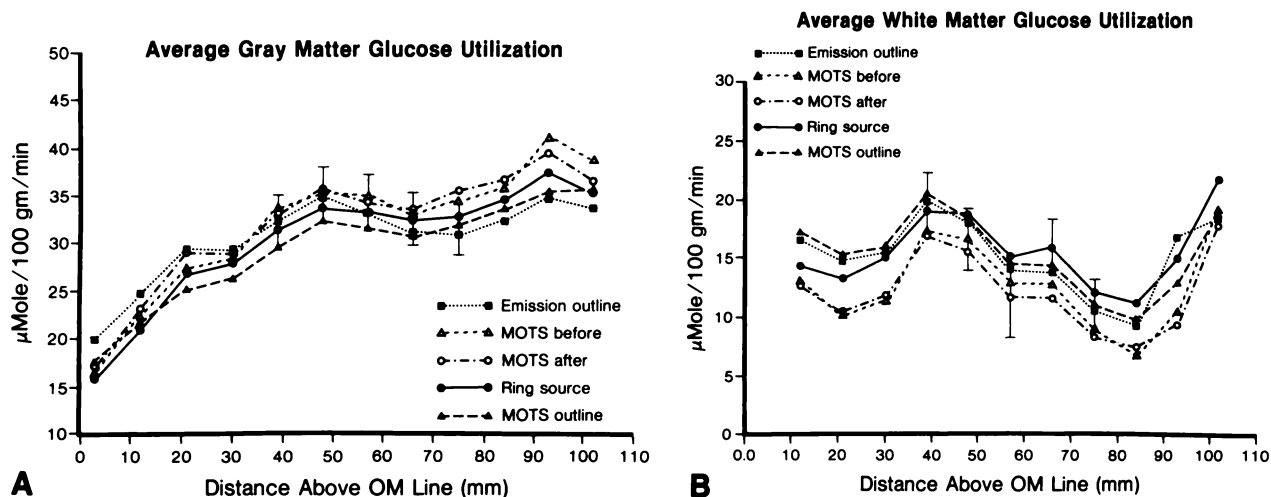
FIGURE 7
Measured average glucose utilization rates in (A) gray matter and mixed regions, (B) white matter regions as a function of distance above OM line for five attenuation correction techniques.

DISCUSSION

The Monte Carlo simulations of four transmission sources demonstrate the MOTS technique provides more coincident counts for a given source activity. It also yields a lower singles rate for a given coincident count rate than other orbiting source and hence a lower deadtime in detectors that are close to it. This reduction in deadtime would be even more significant if the technique were used on the newer commercial PET scanners which have much bigger detector blocks than this system. If the source procurement cost were based on the total activity the MOTS sources would also be cheaper for a given coincident count rate.

In addition to decreased deadtime and random rates, the scatter rejection demonstrated in the MOTS technique improves transmission scan image contrast. The results of the pie phantom studies show that the MOTS transmission images show more contrast and provide more accurate attenuation coefficients than the ring source scans even when performed in the presence of activity concentrations above those commonly observed in patient scans with long-lived isotopes.

The increase in contrast in the MOTS corrected glucose utilization images is probably attributable to the more accurate attenuation correction near the skull. The outer cortical regions are very close to the skull. In the higher slices imaged the skull is quite oblique to the slice, resulting in a greater apparent thickness. Tomitami (7) showed that underestimation of the "skull thickness" has a larger effect on regions very close to the skull. Since the skull attenuation is observed to be higher in the MOTS than ring transmission scans this effect is more pronounced.

Since these studies were done over 50 blood flow and oxygen utilization studies performed on the Positome

have been reconstructed with the outline and MOTS attenuation correction. These studies (to be reported later) show consistently higher functional values in higher outer cortical structures when the MOTS attenuation correction is used.

Some of the MOTS studies presented here show slight ring artifacts. The rings arise from the fact that the detector pairs used in the transmission scan are selected before the "wobble" motion has been encoded. Since our detectors are 2 cm wide, and the "wobble" radius is 1 cm the detector pairs are not really focused on the source as well as they could be. The lead mask surrounding the source no longer fully occludes the detector pair's line of response at the extremes of the wobble cycle. This results in stray radiation, either scattered, or from emission events in the object being scanned, being observed around the edge of the source collimator by a detector pair at during certain parts of the "wobble" cycle. The cyclic inconsistency due to the "wobble" motion gives rise to rings in the image. These artifacts are not intrinsic to the technique, but are the result relatively simple event selection used here and large wobble radius in our scanner.

Selecting the detector pairs after the "wobble" has been encoded, as proposed by the Huesman (12) has eliminated this problem. Since these studies were performed, more lead has been added around the source, and valid events are determined by windowing the sinogram (12,23).

The NIH group (15,16) have also tested the feasibility of doing post injection transmission scans using a ring source (which required the subtraction of 50% of the estimated emission events) and a manually rotated rod source which was not tested on patients. Their phantom experiments showed 5% of the emission events were recorded in their windowed sinograms. The extent of

this contamination depends on the width of the sinogram window, and its impact on image quantification depends also on the relative source intensity. The MOTS technique has the advantage of shielding the detectors currently acquiring a transmission scan from activity in the patient slice under examination. None of the results reported here have been corrected for the activity present in the source at the time the transmission scan was performed. More recently, another set of experiments performed with a narrower sinogram window (23) show that ~0.5% of the events normally acquired in an emission scan are erroneously interpreted as coming from the transmission source.

We have mentioned that this technique should permit simultaneous transmission and emission scans. However, even being able to do the transmission scan immediately after the emission scan is a great advantage, in terms of the time the patient must remain in the scanner, and reducing the possibility of mis-registration of the emission and transmission scans (15). The extension to simultaneous scans would clearly be even better, since registration errors would be eliminated, and patient scan time further reduced. Performing simultaneous emission and transmission scans will also make it unnecessary, when performing a single PET study, to use an immobilizing head holder to ensure slice registration. Patient comfort would undoubtedly be improved, as would scan scheduling in a busy department.

Bailey et al. (24) have shown that simultaneous attenuation correction in some SPECT studies can be done by using a flat sheet source of lower energy gamma rays on the opposite side of the patient to the gamma camera. This has been hailed as a major advance in SPECT quantification (25). These authors acknowledge two problems with their technique (a) contamination of the transmission scan by scattered gamma rays originating in the patient, and (b) the fact that the attenuation values determined by the transmission scan done at a lower energy will be higher than those encountered by gamma rays originating in the patient. Our method suffers to some extent from the former problem, but not the latter, since we are using a positron source.

Since the studies reported here were done we have continued to enhance this technique to allow simultaneous transmission and emission scans. The emission scans are performed at 70% efficiency, since some data along chords near the transmission source must be discarded. Our initial experience with simultaneous transmission and emission scans is reported elsewhere (23).

It is unlikely that simultaneous scans would be practical in rapid studies, e.g., bolus water blood flow or single breath O_2 metabolism studies. These studies are usually done at close to the upper limit of the scanner's normal counting range (6). Simultaneous scans are not necessary with the short scan times (~2 min) used with ^{15}O-labeled tracers. In the course of routine use of this new attenuation technique we have performed transmission scans starting <5 min after the injection of 25 mCi of oxygen-15- (^{15}O) labeled water with no evident contamination due to the rapidly decaying tracer in the patient slice. The transmission scans can thus be performed while the next batch of ^{15}O-labeled compound is being produced, and while the blood samples from the previous study are being counted.

CONCLUSION

We have introduced and evaluated a new technique for performing attenuation correction in PET. Simulations have shown the MOTS technique uses the transmission source's activity more efficiently than if it were in the form of a rod. This results in lower random rates, deadtime, and reduced radiation exposure for a given true coincidence count rate. It has been shown to provide more accurate attenuation measurements than ring source techniques, even in the presence of significant isotope concentrations in the scanner's field of view. This permits transmission scans to be performed after the injection of a long-lived tracer, without compromising the attenuation measurement. The regional differences in observed glucose utilization rates using the new technique appear to be a result of undercompensation of the bone attenuation when using other correction techniques. The improved quantification provided by this technique and the advantage of performing the transmission scan postinjection of long-lived tracers clearly justify its use in routine PET imaging.

ACKNOWLEDGMENTS

REFERENCES

1. Dahlbom M, Hoffman EJ. Problems in signal-to-noise ratio for attenuation correction in high resolution PET. IEEE Trans Nucl Sci 1987; NS-34:288–393.
2. Huang S-C, Hoffman EJ, Phelps ME, Kuhl DE. Quantitation in positron emission tomography: 2. Effects of inaccurate attenuation correction. J Comput Assist Tomogr 1979; 3:804–814.

3. Thompson CJ, Yamamoto YL, Meyer E: Positome II. A high efficiency positron imaging device for dynamic brain studies. *IEEE Trans Nucl Sci* NS-26:583–589.

4. Bergstrom M, Litton J, Erikson L, Bohm C. Determination of object contour from projections for attenuation correction in cranial positron emission tomography. *J Comput Assist Tomogr* 1982; 6:365–372.

5. Cooke BE, Evans AC, et al. Performance figures and images from the Therascan 3128 positron emission tomography. *IEEE Trans Nucl Sci* 1984; NS-31:640–644.

6. Thompson CJ, Dagher A, Meyer E, Evans AC. Imaging performance of a dynamic positron emission tomograph: Positome IIIp. *IEEE Trans Med Imag* 1986; MI-5:184–198.

7. Tomitami T. An edge detection algorithm for attenuation correction in emission CT. *IEEE Trans Nucl Sci* 1988; NS-34:309–312.

8. Johns HE, Cunningham JR. The physics of radiology, (fourth edition). Springfield, IL: Thomas, 1983.

9. International commission on radiological protection: report of the task group on reference man. ICRP, New York: Permagon Press, 1975.

10. Carroll LR, Kertz P, Orcut G. The orbiting rod source: improving performance in Pet transmission correction scans. In: *Emission computed tomography; current trends.* New York: The Society of Nuclear Medicine, 1983.

11. Cahoon JL, Huesman RH, Derenzo SE, et al. The electronics for the Donner 600-crystal positron tomograph. *IEEE Trans Nucl Sci* 1986; NS-33:570–574.

12. Huesman RH, Derenzo SE, Cahoon JL, et al. Orbiting transmission source for positron tomography. *IEEE Trans Nucl Sci* 1988; NS-35:735–739.

13. Thompson CJ, Dagher A, et al. A technique to reject scattered radiation in PET transmission scans. In: Nalcioglu O, Cho ZH, Budinger TF, eds. *International workshop on physics and engineering of computerized multidimensional imaging and processing.* Proc SPIE-671: 1986; 244–253.

14. Dagher A, Thompson CJ. Real-time data rebinning in PET to obtain uniformly sampled projections. *IEEE Trans Nucl Sci* 1985; NS-32:811–817.

15. Daube-Witherspoon M, Carson RE, Green MV. Post-injection transmission attenuation measurements for PET. *IEEE Trans Nucl Sci* 1988; NS-35:757–761.

16. Carson RE, Daube-Witherspoon M, Green MV. A method for post-injection PET transmission measurements with a rotating source. *J Nucl Med* 1988; 29:1558–1567.

17. Thompson CJ. The effect of collimation on scatter fraction in multi-slice *PET. IEEE Trans Nucl Sci* 1988; NS-35:598–602.

18. Chan B, Bergstrom M, Palmer MR, Sayre C, Pate BD. Scatter distribution in transmission measurements with positron emission tomography. *J Comput Assist Tomogr* 1986; 10:296–301.

19. Cooke BE, Evans AC. A phantom to assess quantitative recovery of positron tomographs. *J Comput Assist Tomogr* 1983; 7:876–880.

20. Evans AC, Beil C, Marrett, et al. Anatomical-functional correlation using an adjustable MRI-based region-of-interest atlas with positron emission tomography. *J Cereb Blood Flow* 1988; 8:513–530.

21. Evans AC, Diksic M, Yamamoto YL, et al. Effect of vascular activity in the determination of rate constants for the uptake of ^{18}F-labeled 2-Fluoro-2-deoxyglucose: error analysis and normal values in older subjects. *J Cereb Blood Flow Metab* 1986; 6:724–738.

22. Kubler WK, Ostertag H, Hoverath H, et al. Scatter suppression by using a rotating pin source in PET transmission measurements. *IEEE Trans Nucl Sci* 1988; NS-35:749–752.

23. Thompson CJ, Ranger NT, Evans AC. Simultaneous transmission and emission scans in positron emission tomography. *IEEE Trans Nucl Sci* 1989; NS-36: 1011–1016.

24. Bailey DL, Hutton BF, Walker PJ. Improved SPECT using simultaneous emission and transmission tomography. *J Nucl Med* 1987; 28:844–851.

25. Murphy PH. Quantitative emission tomography [Editorial]. *J Nucl Med* 1987; 28:922–923.